Optics and Lasers in Engineering 161 (2023) 107370

Contents lists available at ScienceDirect

Optics and Lasers in Engineering

journal homepage: www.elsevier.com/locate/optlaseng

Optical design of athermalized infrared dual-band annular folded lens with multilayer imaging diffractive optical elements

Jianing Wang [a], Mingxu piao [b,*], Yuanming Zhao [c], Bo Zhang [b]

[a] Changchun Institute of Optics, Fine Mechanics and Physics, Chinese Academy of Sciences, Changchun 130033, China
[b] School of Opto-Electronic Engineering, Changchun University of Science and Technology, Changchun 130022, China
[c] The 27th Research Institute of CETC, Zhengzhou 450047, China

ARTICLE INFO

Keywords:
Annular folded lens
Infrared dual-band
Imaging diffractive optical element
Temperature

ABSTRACT

In order to realize the miniaturization of the infrared dual-band imaging system, a common optical path annular folded lens (AFL) with multilayer imaging diffractive optical element (MIDOE) is designed in this paper. The design principle of the AFL is studied, and the relationship between the obscuration ratio and the field of view is given. For the wide temperature range, the theoretical model of the optimal substrate materials selection for the MIDOE is established to achieve the high diffraction efficiency. According to theory analysis, the infrared dual-band AFL with IRG26-ZNS MIDOE is designed in the mid-wave infrared (MWIR) 3~5 μm and long-wave infrared (LWIR) 8~12 μm. The focal length is 50 mm, the equivalent F number is 1, and the full field of view is 14 ° The modulation transfer function (MTF) curves of each field of view are close to the diffraction limit when the spatial frequency is 20lps/mm, and the MTF values are greater than 0.61 and 0.28 in MWIR and LWIR, respectively. When the ambient temperature ranges from -40 °C to 80 °C, the high image quality is achieved in dual-band. In addition, the tolerance analysis is performed to verify machinability of the system. The research in this paper has important significance for the realization of a new generation of the low-cost, integrated dual-band imaging system.

1. Introduction

As the development of thermal imaging system, the multiband lenses are increasingly used in target detection, such as reconnaissance system, space remote sensing system and so on [1]. When the imaging waveband increases, the corrections of monochromatic and chromatic aberrations are difficult because of the available optical materials are limited. In order to achieve the high image quality, there are various methods to achieve multiband imaging, such as spectroscopic element [2,3], special optical materials [4], freeform prism [5]. When a spectroscopic element is used for multiband imaging, a common aperture optical system is usually used, and the focusing system is added in front of the detectors for each waveband. This multiband imaging system is composed of multiple optical elements, which increases the complexity of the system and cannot realize the miniaturization. For the special optical materials or freeform prism, the processing difficulties limit the application of such systems, and they are too expensive to cannot be mass-produced. In recent years, the metalens has been developed to achieve the single element imaging [6,7]. However, the metalens applied in the infrared multiband is not studied. In addition, most of the currently developed metalenses are in the micron scale and difficulty in manufacturing.

The annular folded lens (AFL) is composed of a single material, and multiple concentric aspheric reflective surfaces are processed on the two sides of lens [8,9]. Compared with the conventional refractive system, the optical length is significantly shortened, and it can be easily processed by the single point diamond turning (SPDT). Because of the singularity of the AFL material, the chromatic aberration cannot be corrected, so the image quality is seriously affected in multiband. The imaging diffractive optical element (IDOE) has special dispersion properties. When the IDOE is combined with the refractive optical element, the chromatic aberration can be corrected, and the system structure is simplified [10–13]. Therefore, the IDOE can be introduced in the AFL to improve the image quality [14]. However, the high image quality only achieved in a narrow waveband when the single-layer IDOE is applied. The main reason is that the diffraction efficiency of the single-layer IDOE will be significantly declined with the imaging wavelength deviating from the design wavelength, so the modulation transfer function (MTF) will be seriously affected in broad or multiband.

Compared with the single-layer IDOE, the multilayer IDOE (MIDOE) has high diffraction efficiency in multiband while maintaining special dispersion properties [15,16]. Therefore, a miniaturized dual-band system with high image quality can be realized combining the MIDOE with

* Corresponding author.
E-mail address: piaomingxu123@126.com (M. piao).

https://doi.org/10.1016/j.optlaseng.2022.107370
Received 14 June 2022; Received in revised form 31 October 2022; Accepted 31 October 2022
Available online 10 November 2022

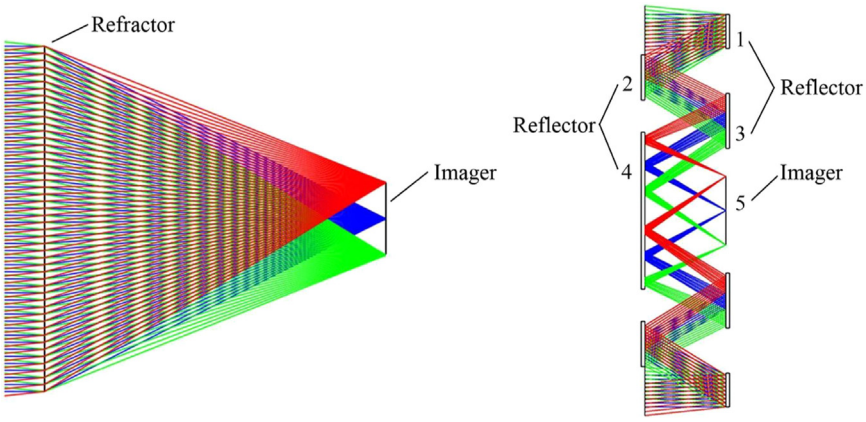

Fig. 1. The principle and structure of the AFL. (a) Refraction structure; (b) Annular folded imaging structure.

the AFL, and the design principle of the hybrid AFL with MIDOE is analyzed in this paper. Since infrared dual-band optical systems are commonly applied in complex environment, the effect on the diffraction efficiency of the MIDOE must be considered. In order to maintain high diffraction efficiency in wide temperature range, The method of the substrate material selection for the dual-band MIDOE is given. According to the theoretical study, the design of the hybrid AFL with MIDOE is completed in mid-wave infrared (MWIR) and long-wave infrared (LWIR) dual-band. The thermal analysis and tolerance analysis are given to verify the feasibility of the designed system.

2. Design principle

The AFL is the extension of the concentric reflective system. The imaging beam is entered through the outer ring aperture of the AFL, and then focused on the detector located in the center of the AFL after passing through a series of concentric annular reflection areas. The principle of the AFL is shown in Fig. 1.

The paraxial refractive optical path of the AFL is shown in Fig. 1(a), and the axial size can be significantly reduced by introducing multiple mirrors, as shown in Fig. 1(b). The axial length of the AFL can be calculated by the following expression [9]

$$t = \frac{f' \cdot n_s}{R_{number}}, \tag{1}$$

where f' is the focal length of the AFL, n_s is refractive index of the substrate material, R_{number} is number of reflections. The axial size of the AFL is smaller with the increase of the R_{number} when the f' and n_s are determined. On the other hand, the outer diameter and volume of the AFL will also increase significantly. Therefore, the four-reflection structure of the AFL is used by analyzing the axial size and outer diameter [14, 17]. Because of the multiple folding and reflection of the optical path, the imaging beam will be intercepted by the central area of the system. The central obscuration ratio is expressed as [18]

$$\alpha_{obs} = \frac{d}{D}, \tag{2}$$

where d is the diameter of obscuration area, D is the outer diameter of the AFL. In order to make the imaging beams in each field of view reflect through multiple annular reflection surfaces to reach the detector without vignetting, the relationship between obscuration ratio and the field of view is obtained as follows

$$\alpha_{obs} = \frac{3}{4} + \frac{7f' \tan(\omega)}{8D}, \tag{3}$$

where ω is the half field of view. When the Eq. (2) is substituted into Eq. (3), the expression can be written as

$$d = \frac{3D}{4} + \frac{7f' \tan(\omega)}{8}, \tag{4}$$

It can be seen from Eq. (4) that the diameter of the central obscuration area will increase as the field of view increases when the outer diameter of the AFL is given, and further, the range of the imaging beam will decrease. In order to increase the area of the annular imaging zone, the outer diameter must be larger, but the weight and size of the AFL are not acceptable. Based on the above design theory, an optical system model with only one reflecting surface can be built at first, and then three reflecting surfaces can be gradually added with equal lengths. The medium between each reflective surfaces is replaced from air to an optical material, and the optical power of the four reflective surfaces are assigned. The focal length and axial size of the AFL are guaranteed by optimizing the radii of the reflective zone surfaces. In order to correct the monochromatic aberration of the AFL, the surface type of each annular zone is aspherical surface. For the chromatic aberration of the AFL, especially multiband, the MIDOE is introduced to improve imaging quality. Since the AFL has only two refractive surfaces, that is the incident annular surface and the exit annular surface, the double-layer IDOE can be formed by adding another material to the outside of these two surfaces, as shown in Fig. 2.

As shown in Fig. 2(a), the double-layer MIDOE is arranged on the incident surface. In order to match the incident surface of the AFL, it is necessary to process another substrate material into a ring shape. Because of the large diameter, it is not only difficult to process, but the weight of the system is increased. In contrast, the MIDOE is arranged on the exit surface to ensure that another material will not affect the stability of the system. In addition, the lateral color is the main aberration that affects the image quality of the AFL, so the best position of the MIDOE should be far from the stop, as shown in Fig. 2(b).

When the ambient temperature of the infrared dual-band optical system changes, the microstructure height and material index of MIDOE will also change, and further, the diffraction efficiency of the MIDOE will be declined [19]. It is necessary to reduce or eliminate the decline in diffraction efficiency over a wide temperature range through optimal selection of substrate materials. In diffractive-refractive hybrid optical system, the actual MTF can be approximated as the product between the polychromatic integral diffraction efficiency (PIDE) for the IDOE and the theoretical MTF, which can be expressed as [16]

$$MTF(\upsilon_x, \upsilon_y) = \bar{\eta}_{PIDE} \cdot MTF_t(\upsilon_x, \upsilon_y), \tag{5}$$

where υ_x and υ_y are the spatial frequencies. The higher $\bar{\eta}_{PIDE}$ represents the less reduction of imaging quality. According to the scalar approximation theory, the expression of $\bar{\eta}_{PIDE}$ for the dual-band can be written as [20]

$$\bar{\eta}_{PIDE} = \frac{w_1}{\lambda_{1\max} - \lambda_{1\min}} \int_{\lambda_{1min}}^{\lambda_{1max}} \eta_m(\lambda, T) d\lambda + \frac{w_2}{\lambda_{2\max} - \lambda_{2\min}} \int_{\lambda_{2min}}^{\lambda_{2max}} \eta_m(\lambda, T) d\lambda, \tag{6}$$

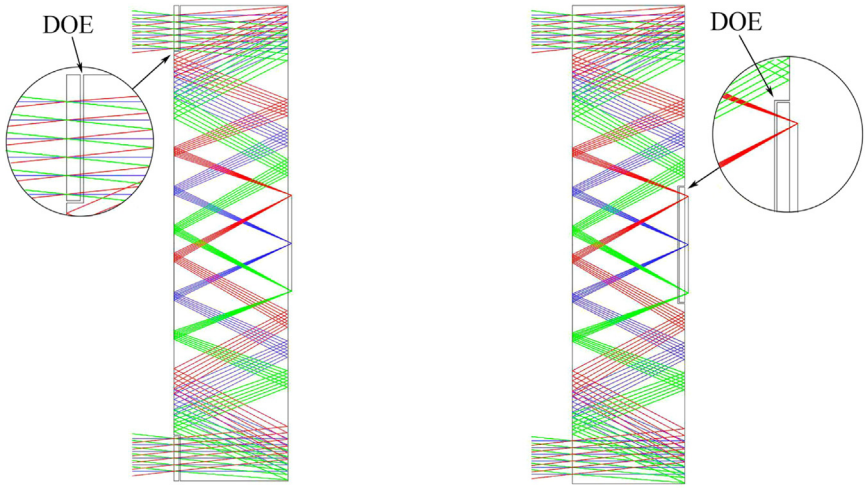

Fig. 2. Schematic diagram of the AFL about the position of double-layer IDOE. (a) Incident Surface; (b) Exit Surface.

where w_1 and w_2 are the weights of the PIDE for the first and second waveband, $\lambda_{1\,\min}$, $\lambda_{1\max}$, $\lambda_{2\,\min}$and $\lambda_{2\max}$are the minimum and maximum wavelengths for the first and second waveband. The diffraction efficiency considering the ambient temperature is

$$\eta_m(\lambda, T) = \sin c^2[m - \phi(\lambda, T)], \tag{7}$$

where $\sin c(x) = \sin(\pi x)/(\pi x)$. m is the diffraction order, usually m is 1. $\phi(\lambda, T)$ is the phase retardation, which can be written as

$$\phi(\lambda, T) = k\left\{ H_1\left[(1+\alpha_1\Delta T)(n_1(\lambda)-1) + \frac{dn_1}{dT}\Delta T\right] + H_2\left[(1+\alpha_2\Delta T)(n_2(\lambda)-1) + \frac{dn_2}{dT}\Delta T\right]\right\}, \tag{8}$$

where k is the wave number. H_1 and H_2 are the microstructure heights of the first and the second harmonic diffractive elements (HDEs) [21], respectively. $n_1(\lambda)$ and $n_2(\lambda)$ are the refractive indices of two substrate materials, respectively. α_1 and α_2 are the thermal expansion coefficients of the first and the second HDEs, respectively. $\frac{dn_1}{dT}$ and $\frac{dn_2}{dT}$ are the thermo-optic coefficients of the first and the second HDEs, respectively. ΔT is the difference between the arbitrary ambient temperature T_a and the design temperature T_d, which is $\Delta T = T_a - T_d$. In order to achieve 100% diffraction efficiency in Eq. (7), $\phi(\lambda, \theta)$ is equal to 1, the microstructure heights can be obtained as

$$\begin{aligned} H_1 &= \frac{\lambda_{d2}B(\lambda_{d1}) - \lambda_{d1}B(\lambda_{d2})}{A(\lambda_{d2})B(\lambda_{d1}) - A(\lambda_{d1})B(\lambda_{d2})}, \\ H_2 &= \frac{\lambda_{d1}A(\lambda_{d2}) - \lambda_{d2}A(\lambda_{d1})}{A(\lambda_{d2})B(\lambda_{d1}) - A(\lambda_{d1})B(\lambda_{d2})} \end{aligned}, \tag{9}$$

where

$$\begin{aligned} A(\lambda) &= (1+\alpha_1\Delta T)(n_1(\lambda)-1) + \frac{dn_1}{dT}\Delta T \\ B(\lambda) &= (1+\alpha_2\Delta T)(n_2(\lambda)-1) + \frac{dn_2}{dT}\Delta T \end{aligned}, \tag{10}$$

where λ_{d1} and λ_{d2} are two design wavelengths. For the dual-band imaging system, λ_{d1} is selected in the first waveband, and λ_{d2} is selected in the second waveband. Because of the thermal parameters of substrate materials are considered in Eq. (9), the optimal microstructure heights can be calculated to achieve the maximum PIDE in an arbitrary temperature. When the MIDOE is applied in wide temperature range, the comprehensive PIDE difference $\Delta\bar{\eta}_{PIDE}(\lambda)$ can be calculated as follows

$$\Delta\bar{\eta}_{PIDE}(\lambda) = \bar{\eta}^{T_d}_{PIDE}(\lambda) - \bar{\eta}^{T_a}_{PIDE}(\lambda), \tag{11}$$

where $\bar{\eta}^{T_d}_{PIDE}(\lambda)$ and $\bar{\eta}^{T_a}_{PIDE}(\lambda)$ are the PIDE at the design temperature T_d and an arbitrary ambient temperature T_a. When the substrate material combination is selected, the thermal properties of two substrate materials are determined, so $\bar{\eta}^{T_d}_{PIDE}(\lambda)$ and $\bar{\eta}^{T_a}_{PIDE}(\lambda)$ are unique. Therefore, the smaller $\Delta\bar{\eta}_{PIDE}(\lambda)$ indicates that the selected material combination has less PIDE reduction, and the high MTF can be achieved over a wide temperature range.

Table 1
Design specifications of the infrared dual-band AFL .

Parameters	Values
Focal Length	50mm
Effective F number	1
Full field of view	14°
Axial length	≤25mm
Wavelength	3~5 μm, 8~12μm
Ambient temperature range	−40~80 °C

3. Examples and analysis

As an example, an AFL with double-layer IDOE is designed for the MWIR-LWIR dual-band. The focal length is 50 mm, and the F number is 1. The design specifications are listed in Table 1. For the substrate material of the AFL, it is not only necessary to satisfy the transmittance of the MWIR and LWIR, but the thermal and processing properties should be considered.

3.1. Optimal substrate material combination in wide temperature range

In order to reduce the influence of a wide temperature range on the diffraction efficiency of the MIDOE, the optimal substrate material combination should be selected for a given waveband and temperature range. In the MWIR and LWIR, the available materials include Germanium (Ge), Zinc Selenide (ZNSE), Zinc Sulfide (ZNS), AMTIR1 [22], Gallium Arsenide (GAAS) [23], chalcogenide glass IRG26 [24]. The thermal parameters for these materials are listed in Table 2.

In the MWIR-LWIR dual-band, the $\bar{\eta}_{PIDE}$ can be calculated by Eq. (6) for the determined substrate material combination, and corresponding optimal microstructure heights can be obtained by Eq. (9) and Eq. (10). When the design temperature T_d is 20 °C and an arbitrary ambient temperature T_a is 60 °C, the comprehensive PIDE difference $\Delta\bar{\eta}_{PIDE}(\lambda)$ can be calculated by Eq. (11). The relationship between the $\bar{\eta}_{PIDE}$ and ambient temperature is shown in Fig. 3, and the $\Delta\bar{\eta}_{PIDE}(\lambda)$ for various combinations are listed in Table 3.

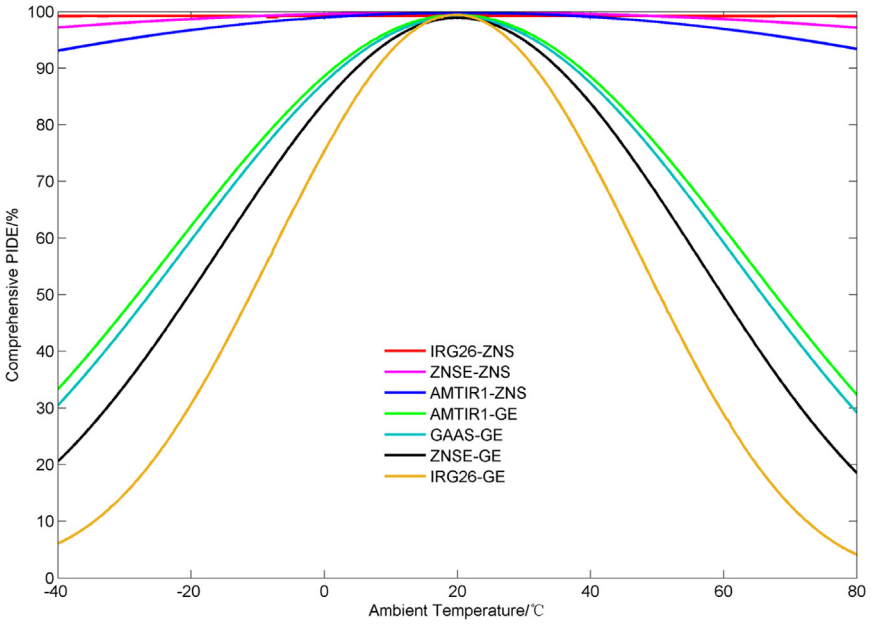

Fig. 3. Comprehensive PIDE of the various substrate material combinations in MWIR-LWIR dual-band.

Table 2
Thermal Parameters for Infrared Materials .

Material	$\alpha(\times10^{-6}/$ °C)	dn/dT ($\times10^{-6}/$ °C)	
		MWIR	LWIR
GE	5.7	424	404
ZNSE	7.1	63	61
ZNS	6.6	43.3	39
AMTIR1	12	72	72
GAAS	5.8	200	200
IRG26	20.8	34.3	32.2

Table 3
Comprehensive PIDE difference for various substrate material combinations in the MWIR-LWIR dual-band .

Substrate Material Combination	$\Delta\overline{\eta}_{PIDE}(\lambda)$ (%)
IRG26-ZNS	0.011
ZNSE-ZNS	0.640
AMTIR1-ZNS	1.538
AMTIR1-GE	21.339
GAAS-GE	23.707
ZNSE-GE	26.399
IRG26-GE	50.992

As shown in Fig. 3, The comprehensive PIDEs of the IRG26-ZNS MIDOE, ZNSE-ZNS MIDOE and AMTIR1-ZNS MIDOE are less affected by ambient temperature, while other combinations are significantly affected by ambient temperature. Among above three combinations, the comprehensive PIDE change of the IRG26-ZNS MIDOE is the steadiest, and the $\Delta\overline{\eta}_{PIDE}(\lambda)$ is only 0.011%, as listed in Table 3. It is noted that some combinations are not analyzed, because the calculated microstructure heights are too large for processing.

3.2. Design of the dual-band AFL with double-layer MIDOE

According to the analysis in Section 3.1, the IRG26-ZNS MIDOE is the best combination in the wide ambient temperature. The chalcogenide glass material IRG26 ($As_{40}Se_{60}$) has excellent thermal characteristics and dispersion characteristics. At the same time, the IRG26 can be processed by the precision molding [25], which is beneficial to reduce the processing cost. Therefore, the IRG26 is selected as the main optical material of the AFL.

When the substrate material of the AFL is determined, the initial parameters can be calculated by the design specifications in Table 1. The number of folds affects the volume and size of the AFL, and the four-reflection structure is selected [14]. According to the focal length, the initial axial length of the AFL t is 34.9 mm when the R_{number} is 4. The relationship between obscuration ratio α_{obs} and the outer diameter D as shown in Fig. 4.

The outer diameter of the AFL increases rapidly when the obscuration ratio is greater than 0.7, which will cause the volume and size of the AFL to increase significantly, so the initial selection of α_{obs} is 0.7. Substitute the focal length, field of view and α_{obs} into Eq. (3), and the initial D and $d$are 107.4 mm and 75.2 mm, respectively. Based on the calculation results of the above parameters, a reflective AFL structure is built at first, and the air between each reflective surface is replaced with the substrate material IRG26. In order to correct the monochromatic aberration of the system, the annular surface type is set to the even asphere which can be written as [26]

$$z = \frac{cr^2}{1+\sqrt{1-(1+k)c^2r^2}} + \sum_{i=1}^{8} a_i r^{2i}, \tag{12}$$

where z is the sag of aspheric surface, c is the curvature, k is the conic constant, r is the radial height. For the AFL, the middle medium of two multiple concentric reflective surfaces is a type of optical material, so the chromatic aberration exists and cannot be corrected by surface parameter optimization. Because of the optical power of the first refractive surface is commonly weak, the axial chromatic aberration is not main aberration to reduce the image quality. However, the lateral color aberration is the main aberration which significantly affects the image quality of the AFL [14]. At this time, a ZNS lens is added at the position of the exit surface to realize the MIDOE, and the influence of chromatic aberration can be eliminated. In the zemax, the surface type of Binary2 is selected as the diffractive element, and the phase expression can be written as [26]

$$\phi_{B2}=m\sum_{i=1}^{N} A_i \rho^{2i}, \tag{13}$$

where A_i is the coefficient of polynomial, ρ is the normalized radial height. When the annular radii, aspheric coefficients, thicknesses, and

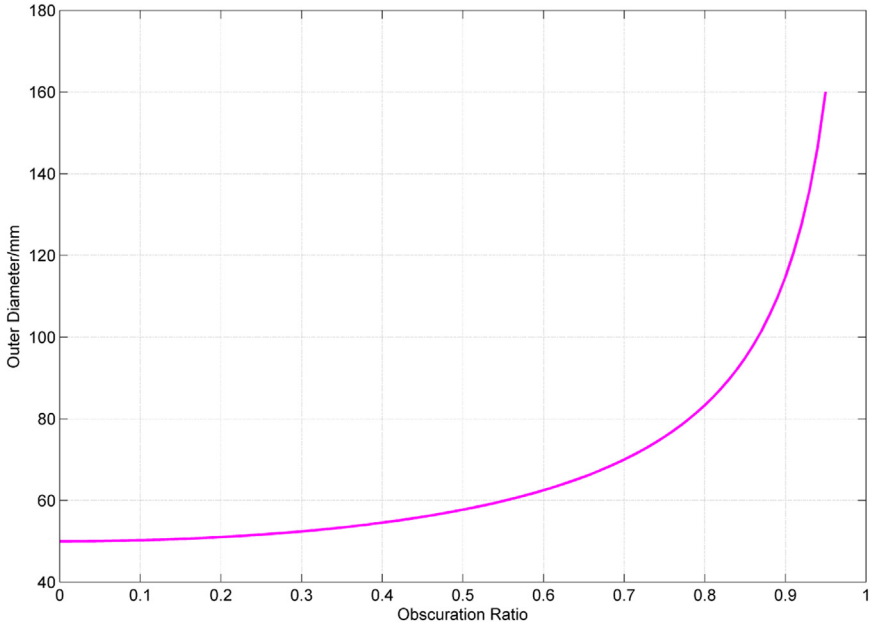

Fig. 4. The obscuration ratio versus the outer diameter.

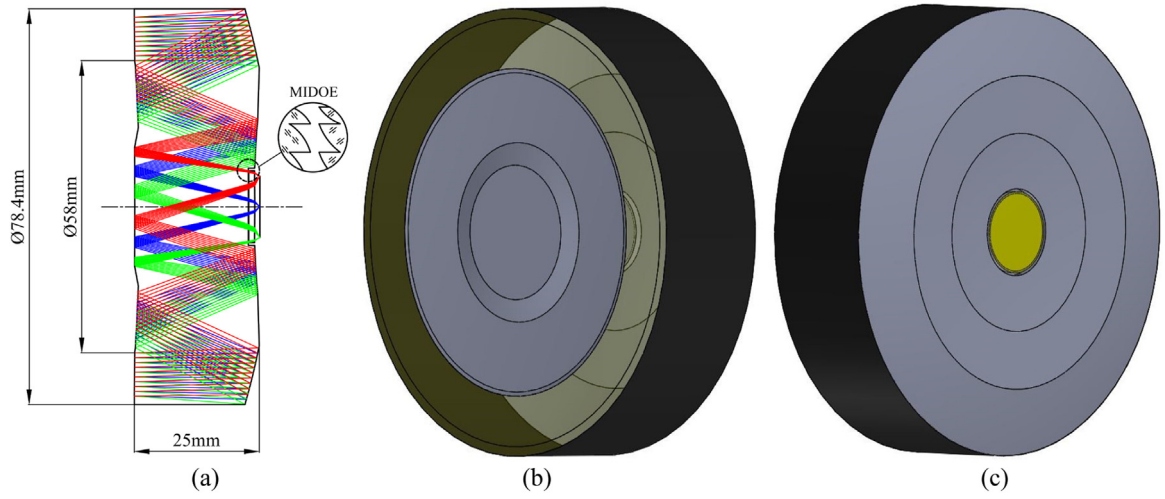

Fig. 5. Infrared dual-band AFL with double-layer IDOE. (a) System layout; (b) Front view of the solid model; (c) Rear view of the solid model.

coefficients of phase polynomials are optimized, the final structure is obtained as shown in Fig. 5.

The effective aperture of the infrared dual-band AFL is 50 mm, the outer aperture is 78.4 mm, the obscuration ratio is 0.74, and the axial length is 25 mm after optimization. In Fig. 5(b) and 5(c), the yellow area represents the refractive zone, and the gray area represents the reflective zone. The MTF curve of the system is shown in Fig. 6.

As shown in Fig. 6, the MTF values are greater than 0.61 and 0.28 in MWIR and LWIR when the spatial frequency is 20 lps/mm, respectively. It is noted that the MTF value of the LWIR is smaller than that of the MWIR. The reason is that the cutoff frequency of the LWIR is smaller for the common path AFL [15], so the diffraction-limited curve of the LWIR is lower than the MWIR at 20lps/mm. The phase distribution generated by the double-layer IDOE is divided by 2π, and the diffractive zones can be obtained. When the refractive index and thermal parameters of the two substrate materials are substituted into the Eq. (6), the optimal design wavelengths are 3.79 μm and 10.23 μm. The corresponding optimal microstructure heights can be calculated by Eq. (9) in design temperature, that is 104.92 μm and 147.27 μm for IRG26 and ZNS, respectively. The microstructure heights are shown in Fig. 7, and the period radius of the MIDOE is listed in Table 4. The minimum period width is 1.16 mm, and microstructure can be easily processed by the SPDT.

Table 4
Period radius of IRG26-ZNS MIDOE .

Period ring	Radial radius(mm)
1	3.66
2	5.18
3	6.34

3.3. Thermal analysis

The thermal analysis of the MWIR-LWIR dual-band AFL is given in temperature range of −40 °C~80 °C. According to the calculated parameters of the IRG26-ZNS MIDOE, the relationship among temperature, wavelength and diffraction efficiency is shown in Fig. 8. The results show that the diffraction efficiency of the IRG26-ZnS MIDOE is less af-

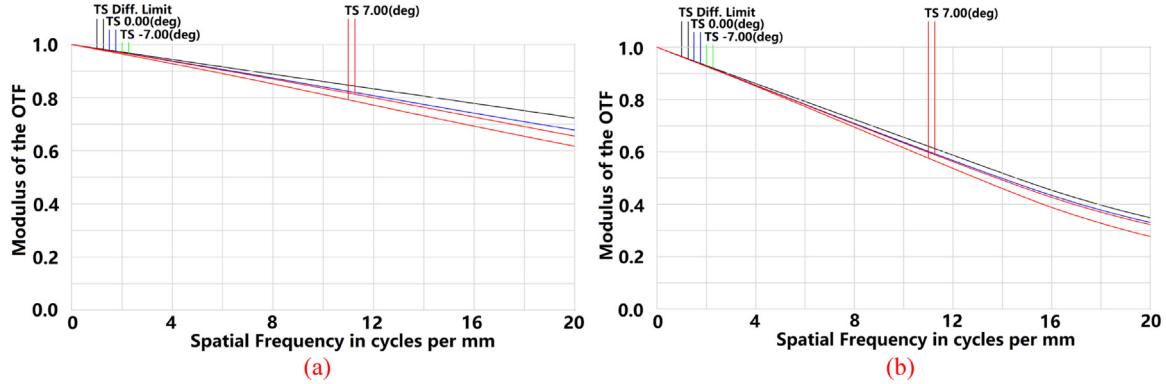

Fig. 6. MTF curve of infrared dual-band AFL with MIDOE. (a) MWIR; (b) LWIR.

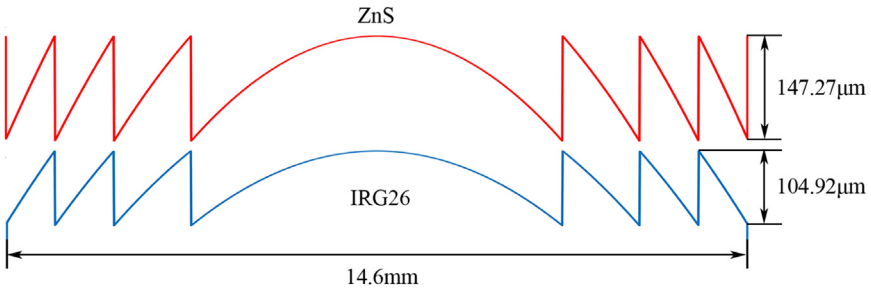

Fig. 7. Microstructure of the IRG26-ZNS MIDOE.

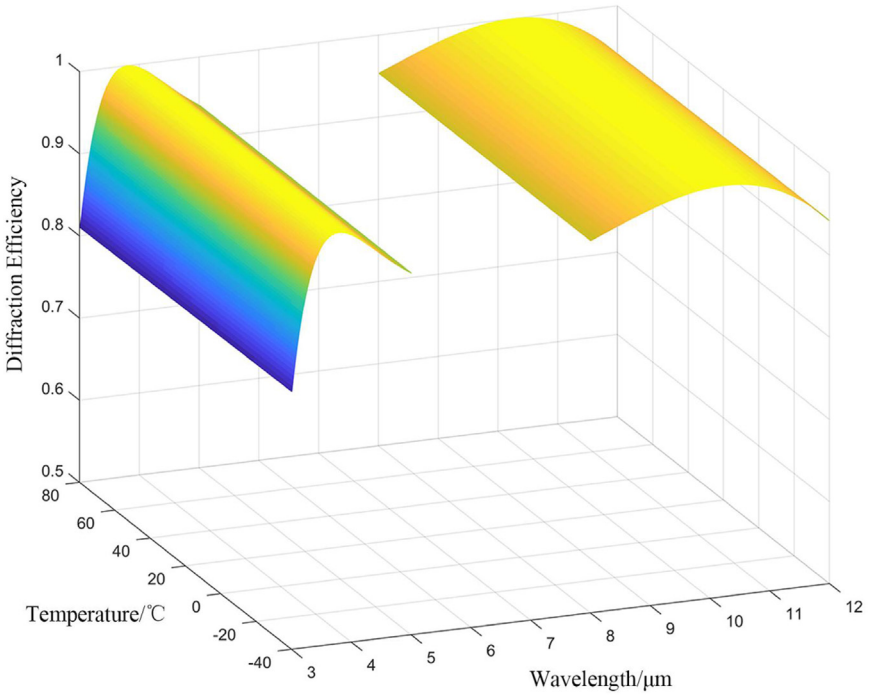

Fig. 8. Diffraction efficiency varies with temperature and wavelength for the IRG26-ZNS MIDOE .

fected by temperature change, and the impact on the imaging quality of the hybrid AFL system is negligible.

When the ambient temperatures are −40 °C, 20 °C and 80 °C, the parameters of the AFL with the MIDOE are optimized. The MTF curves at −40 °C, 20 °C and 80 °C are shown in Fig. 9, and the minimum MTF values of different temperatures are listed in Table 5.

It can be seen from Table 5, the minimum MTF values of −40 °C, 20 °C and 80 °C are higher than 0.60 in the MWIR. In the LWIR, the minimum MTF values at −40 °C, 20 °C and 80 °C are close to 0.30. The results show that the AFL with IRG26-ZNS MIDOE is achieved the athermalization in the MWIR-LWIR dual-band.

3.4. Tolerance analysis

For the AFL, the annular refractive or reflective surfaces are processed on the front or rear surfaces of a single substrate material. These annular surfaces are connected by the substrate material and cannot be adjusted. Therefore, the processing of the AFL will impact on the system quality in directly, which is different from traditional refractive or reflective optical systems. The sensitivity tolerances about thickness, eccentricity, tilt and aspheric surface error are analyzed, as listed in Table 6. The back focal length is selected as the compensator.

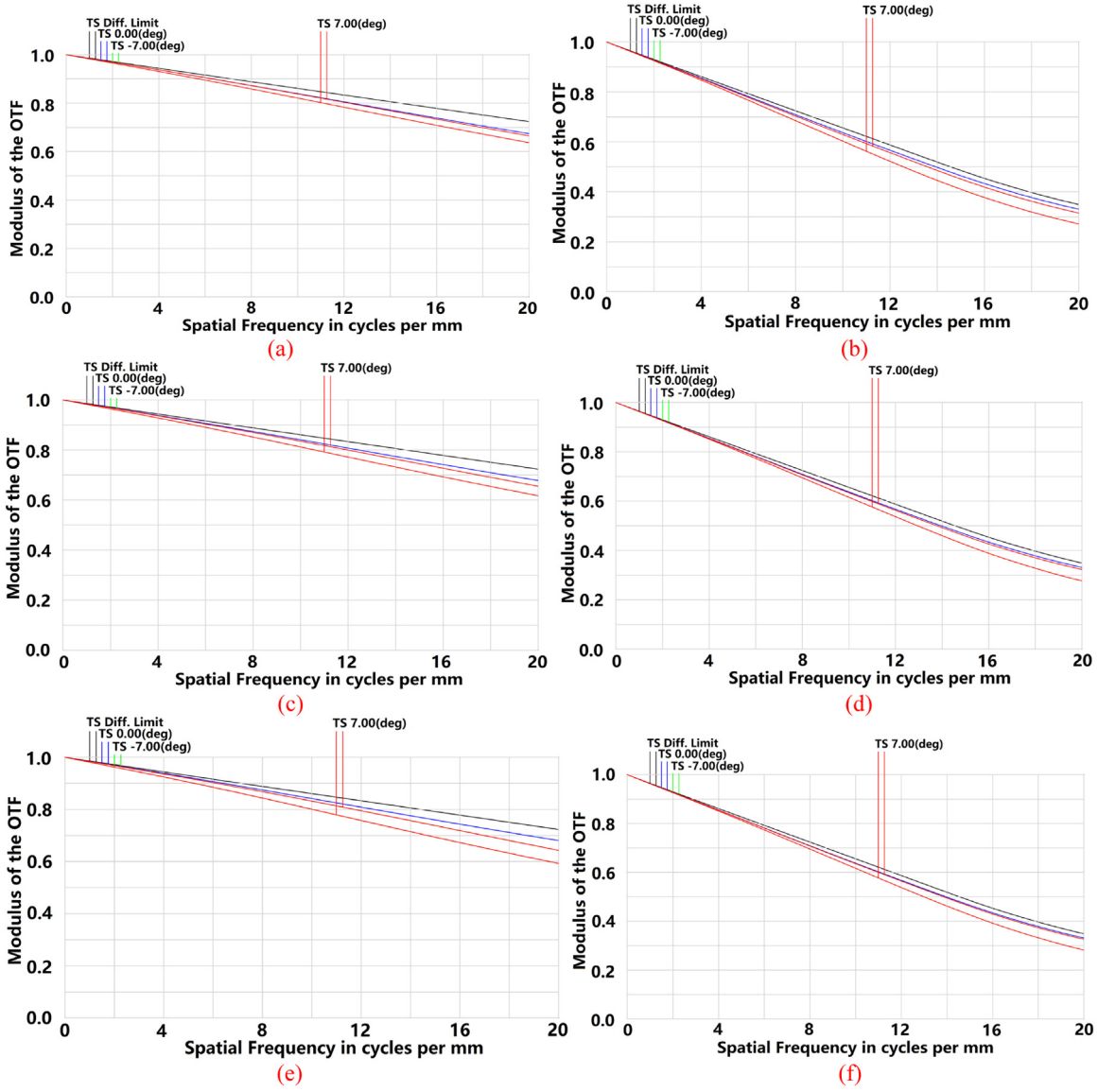

Fig. 9. MTF of infrared dual-band AFL with MIDOE. (a) MWIR at −40 °C; (b) LWIR at −40 °C; (c) MWIR at 20 °C; (d) LWIR at 20 °C; (e) MWIR at 80 °C; (f) LWIR at 80 °C.

Table 5
The minimum MTF at different temperatures for dual-band AFL .

Temperature /°C	3~5μm			8~12μm		
	0°	4.9°	7°	0°	4.9°	7°
−40	0.672	0.644	0.646	0.330	0.296	0.286
20	0.674	0.612	0.612	0.331	0.301	0.288
80	0.677	0.604	0.604	0.331	0.304	0.285

Table 6
Tolerance of the AFL .

Tolerance index	Tolerance value
Thickness(mm)	±0.01
Component eccentricity (mm)	±0.02
Component tilt (′)	±1
Surface eccentricity (mm)	±0.02
Surface tilt (′)	±1
PV value of Aspheric Surface (μm)	±0.2
Refractive index	±0.001
Test wavelength (nm)	632.8

Table 7
System MTF after tolerance analysis.

Wavelength(μm)	Field(°)	Tangential Standard	Analysis	Sagittal Standard	Analysis
3~5	0	0.71	0.56	0.70	0.56
	4.9	0.61	0.49	0.67	0.51
	7	0.61	0.40	0.66	0.46
8~12	0	0.34	0.32	0.36	0.32
	4.9	0.31	0.27	0.33	0.27
	7	0.29	0.24	0.35	0.28

The 1000 times Monte Carlo analysis is performed based on the Table 6. The MTF is used as the evaluation standard, and the results at the spatial frequency of 20 lps/mm is listed in Table 7.

It can be seen from the Monte Carlo analysis in Table 7 that when the spatial frequency is 20 lps/mm in the MWIR, the 90% of the tangential MTF values in the central and edge field of view are greater than 0.56 and 0.40, respectively; the 90% of the sagittal MTF values in the central and edge field of view are greater than 0.56 and 0.46, respectively. For

the LWIR, the 90% of the tangential MTF values in the central and edge field of view are greater than 0.32 and 0.24, respectively; the 90% of the sagittal MTF values of the central and edge field of view are greater than 0.32 and 0.28, respectively. The results show that the tolerances in Table 6 can satisfy the actual processing requirements of the AFL.

4. Conclusions

In this paper, an athermalized AFL with MIDOE is designed for MWIR-LWIR dual-band, and the design method of AFL is given. In order to achieve the high diffraction efficiency in a wide temperature range, a theoretical model for the optimal substrate materials selection of infrared dual-band MIDOE is established. It is found that IRG26 and ZNS are the best combination in MWIR-LWIR dual-band. According to the design specification, the initial parameters of the AFL is calculated, and the hybrid AFL design is realized by the optimization of the annular aspheric surfaces and diffractive phase. The system focal length is 50 mm and the axial length is 25 mm. The MTF values are greater than 0.61 and 0.28 in MWIR and LWIR when the spatial frequency is 20 lps/mm, respectively. In the temperature range of −40 °C~80 °C, the MTF values of each field of view are greater than 0.61 in the MWIR, and are greater than 0.28 in the LWIR. In addition, the tolerances of the AFL are analyzed, and the designed AFL is machinable. The design results of this paper provide new ideas for the realization of the low-cost, miniaturized infrared dual-band imaging systems in the future.

Funding

This work was supported by The National Natural Science Foundation of China Youth Fund (62105041 and 62005268); The Education Department Project of Jilin Province (JJKH20220741KJ and JJKH20220748KJ).

Declaration of Competing Interest

The authors declare that they have no known competing financial interests or personal relationships that could have appeared to influence the work reported in this paper.

CRediT authorship contribution statement

Jianing Wang: Writing – original draft, Formal analysis. **Mingxu piao:** Conceptualization, Methodology, Supervision, Writing – review & editing. **Yuanming Zhao:** Investigation, Formal analysis. **Bo Zhang:** Writing – review & editing, Data curation.

References

[1] Zhang Yiwei, Bibson Graham M, Edgar Matthew P, Hammond Giles, Padgett Miles J. Dual-band single-pixel telescope. Opt Express 2020;28(12):18180–8. doi:10.1364/OE.392522.
[2] Chen Yang, Gao Ming, Song Xiao. Method to design the common aperture multiband optical system based on the PSO algorithm. Opt Express 2021;29(12):18325–35. doi:10.1364/OE.424903.
[3] Yang Gao Ming Chen, Jun Liu, Hong Lv. Design of dual-band shared-aperture co-zoom optical system. Infrared Phys Technol 2014;64:40–6. doi:10.1016/j.infrared.2014.01.014.
[4] Rui Qu, Jian Deng. Methods of correcting between-band chromatic aberration in infrared dual-band dual-field of view athermalized optical design. Acta Optica Sinica 2015;35(1):0122006. doi:10.3788/AOS201535.0122006.
[5] Yu Jun, Shen Zhengxiang, Wang Zhanshan. Compact dual band/dual FOV infrared imaging system with freeform prism. Opt Lett 2021;46(4):829–32. doi:10.1364/OL.412091.
[6] Banerji S, Meem M, Majumder A, Vasquez FG, Sensale-Rodriguez B, Menon R. Imaging with flat optics: metalenses or diffractive lenses? Optica 2019;6(6):805–10. doi:10.1364/OPTICA.6.000805.
[7] Liu K, Lian M, Qin K, Zhang S, Cao T. Active tuning of electromagnetically induced transparency from chalcogenide-only metasurface. Light 2021;2(3):251–61. doi:10.37188/lam.2021.019.
[8] Tremblay Eric J, Stamenov Igor, Dirk Beer R, Arianpour Ashkan, Ford Joseph E. Switchable telescopic contact lens. Opt Express 2013;21(13):15980–6. doi:10.1364/OE.21.015980.
[9] Tremblay Eric J, Stack Ronald A, Morrison Rick L, Karp Jason H, Ford Joseph E. Ultrathin four-reflection imager. Appl Opt 2009;48(2):343–54. doi:10.1364/AO.48.000343.
[10] Kuschmierz R, Scharf E, Ortegón-González DF, Glosemeyer T, Czarske JW. Ultra-thin 3D lensless fiber endoscopy using diffractive optical elements and deep neural networks. Light 2021;2(4):415–24. doi:10.37188/lam.2021.030.
[11] Dun Xiong, Ikoma Hayato, Wetzstein Gordon, Wang Zhanshan, Cheng Xinbin, Peng Yifan. Learned rotationally symmetric diffractive achromat for full-spectrum computational imaging. Optica 2020;7(8):913–22. doi:10.1364/OPTICA.394413.
[12] Zhang H, Liu H, Xu W, Lu Z. Large aperture diffractive optical telescope: a review. Opt Laser Tech 2020;130:106356. doi:10.1016/j.optlastec.2020.106356.
[13] Cheng D, Wang Q, Liu Y, Chen H, Ni D, et al. Design and manufacture AR head-mounted displays: a review and outlook. Light 2021;2(3):350–69. doi:10.37188/lam.2021.024.
[14] Zhang Bo, Piao Mingxu, Cui Qingfeng. Achromatic annular folded lens with reflective-diffractive optics. Opt Express 2019;27(22):32337–48. doi:10.1364/OE.27.032337.
[15] Soskind YG. Diffractive optics technologies in infrared systems. SPIE 2015;9451:94511T. doi:10.1117/12.2176828.
[16] Mao S, Cui Q, Piao M, Zhao L. High diffraction efficiency of three-layer diffractive optics designed for wide temperature range and large incident angle. Appl Opt 2016;55(13):3549–54. doi:10.1364/AO. 55.003549.
[17] Yutong Meng, Mingxu Piao, Qi Wang. Design of refractive diffraction hybrid annular aperture ultrathin imaging optical system. Acta Photonica Sinica 2019;48(12):1211003. doi:10.3788/gzxb2019 4812.1211003.
[18] Smith WJ. Modern optical engineering. 4th ed. New York: McGraw-Hill; 2008.
[19] Piao Mingxu, Cui Qingfeng, Zhu Hao, Xue Changxi, Zhang Bo. Diffraction efficiency change of multilayer diffractive optics with environmental temperature. J Opt 2014;16(3):035707. doi:10.1088/2040-8978/16/3/035707.
[20] Xue C, Cui Q, Liu T, Yang L, Fei B. Optimal design of a multilayer diffractive optical element for dual wavbands. Opt lett 2010;35(24):4157–9. doi:10.1364/OL.35.004157.
[21] Sweeney CW, Sommargren GE. Harmonic diffractive lenses. Appl Opt 1995;34(14):2469–75. doi:10.1364/ao.34.002469.
[22] Bass M, Li G, Stryland EV. Handbook of optics volume IV optical properties of materials, nonlinear optics, quantum optics. 3rd ed. New York: McGraw-Hill; 2010.
[23] Riedl MJ. Optical design fundamentals for infrared systems. 2nd ed. New York: SPIE; 2001.
[24] Infrared Chalcogenide Glasses. http://www.us.schott.com/advanced_optics/english/products/optical-materials/ir-materials/infrared-chalcogenide-glasses/index.html.
[25] Liu Y, Xing Y, Yang C, Li C, Xue C. Simulation of heat transfer in the progress of precision glass molding with a finite element method for chalcogenide glass. Appl Opt 2019;58(27):7311–18.
[26] Zemax Development Corporation OpticStudio user manual; 2016.